Astronomy & Astrophysics manuscript no. main
June 29, 2021

X-Ray Studies of the Abell 3158 Galaxy Cluster with eROSITA

B. Whelan[1], T. H. Reiprich[1], F. Pacaud[1], E. Bulbul[2], M. E. Ramos-Ceja[2], J. S. Sanders[2], J. Aschersleben[1], J. Iljenkarevic[1], A. Veronica[1], K. Migkas[1], M. Freyberg[2], K. Dennerl[2], M. Kara[1,4], A. Liu[2], V. Ghirardini[2], and N. Ota[1,3]

[1] Argelander-Institut für Astronomie (AIfA), Universität Bonn, Auf dem Hügel 71, 53121 Bonn, Germany
e-mail: bwhelan@astro.uni-bonn.de
[2] Max-Planck-Institut für extraterrestrische Physik, Giessenbachstraße 1, 85748 Garching, Germany
[3] Department of Physics, Nara Women's University, Kitauoyanishi-machi, Nara, 630-8506, Japan
[4] Institute for Astroparticle Physics, Karlsruhe Institute of Technology, 76021 Karlsruhe, Germany

Received . . . ; Accepted . . .

ABSTRACT

Context. The most nearby clusters are the best places to study physical and enrichment effects in the faint cluster outskirts. The Abell 3158 cluster (A3158), located at $z = 0.059$ is quite extended with a characteristic radius $r_{200} = 23.95$ arcmin. The metal distribution in the outskirts of this cluster has previously been studied with *XMM-Newton*. In 2019, A3158 was observed as a calibration target in a pointed observation with the eROSITA telescope onboard the Spektrum-Roentgen-Gamma (SRG) mission. Bright large clusters, like A3158, are ideal for studying the metal distribution in the cluster outskirts, along with the temperature profile and morphology. With the deeper observation time of the eROSITA telescope, these properties can be studied in greater detail and at larger radii now. Furthermore, bright nearby clusters are ideal X-ray instrumental cross-calibration targets as they cover a large fraction of the detector and do not vary in time.
Aims. We first aim to compare the temperature, metal abundance and normalisation profiles of the cluster from eROSITA with previous *XMM-Newton* and *Chandra* data. Following this calibration work, we aim to investigate the temperature and metallicity of the cluster out to close to r_{200}, measure the galaxy velocity dispersion, and determine the cluster mass. Furthermore, we aim to search for infalling clumps and background clusters in the field.
Methods. We determined 1d temperature, abundance and normalisation profiles from both eROSITA and *XMM-Newton* data as well as 2d maps of temperature and metal abundance distribution from eROSITA data. The velocity dispersion was determined and the cluster mass was calculated from the mass - velocity dispersion (M_{200} - σ_v) relation. Galaxy density maps were created to get a better understanding of the structure of the cluster and the outskirts.
Results. The overall (i.e., in the range $0.2 - 0.5 r_{500}$) temperature was measured to be 4.725 ± 0.035 keV. The temperature, abundance and normalisation profiles of eROSITA all agree on a $\lesssim 10\%$ level with those we determined using *XMM-Newton* and *Chandra* data; and they are also consistent with the profiles published previously by the X-COP project. The Abell 3158 cluster morphology and surface brightness profile look regular at a first glance. Clusters that have such profiles typically are relaxed and host cool cores. However, from the temperature profile and map we see that the cluster lacks a cool core, as was noted before. Instead, the presence of an off-centre cool clump to the west of the central cluster region, which has been previously detected, is observed. These are indications that the cluster may be undergoing some sloshing and merger activity. Furthermore there is a bow shaped edge near the location of the cool gas clump West of the cluster centre. Further out in the West of the X-ray images of A3158 an extension of gas is detected; the larger scale extension described here for the first time. The velocity dispersion of the cluster member galaxies was measured to be $1058 \pm 41 \mathrm{km\,s^{-1}}$ based on spectroscopic redshifts of 365 cluster member galaxies and the total mass determined as $M_{200,c} = 1.38 \pm 0.25 \times 10^{15} M_\odot$. The mass estimate based on the X-ray temperature is significantly lower at $M_{200} = 5.09 \pm 0.59 \times 10^{14} M_\odot$, providing further indications for merger activity boosting the velocity dispersion and/or biasing the temperature low. An extended X-ray source located in the South of the field of view also coincides with a galaxy overdensity with spectroscopic redshifts in the range $0.05 < z < 0.07$. This source further supports the idea that the cluster is undergoing merger activity. Another extended source located in the North of the field of view is detected in X-rays and coincides with an overdensity of galaxies with spectroscopic redshifts in the range of $0.070 < z < 0.077$. This is likely a background cluster not directly related to A3158. Additionally a known South Pole Telescope (SPT) cluster SPT-CL J0342-5354 at $z = 0.53$ was detected.

Key words. Galaxies: clusters: individual: Abell 3158 - X-rays: galaxies: clusters - Galaxies: clusters: intracluster medium

1. Introduction

As the largest known gravitationally bound objects in the observable universe, galaxy clusters are important for the study of the large scale structure and cosmology. Accretion and merging with smaller objects are the processes in which galaxy clusters grow. Clusters typically have masses between 10^{14} and $10^{15} M_\odot$ consisting of approximately 100 - 1000 galaxies, hot intra-cluster gas, dark matter and a small population of relativistic particles. Clusters can reach sizes of up to 6 Mpc in diameter and are important astrophysical laboratories for the study of metal abundance, temperature, and gas densities of this hot intra-cluster medium. Particularly interesting is the metal abundance in the outskirts of galaxy clusters, i.e. outside r_{500} and inside $3 \sim r_{200}$ (Reiprich et al. 2013). The metal abundance in cluster outskirts is not only useful to estimate the total mass of metals in the current universe, but also retains the information of early enrichment, which reflects the cosmic star formation in early epochs. The low-redshift clusters such as Abell 3158 ($z = 0.059$, Struble

& Rood 1999) are good places to examine the faint outskirts of clusters. The physical and enrichment processes that are absent or less important in the central regions of clusters, such as minor mergers, infall of gas clumps, etc., likely affect the gas in the cluster outskirts (e.g., Reiprich et al. 2013).

The Spektrum Roentgen Gamma (SRG) mission, launched on the 13th of July 2019 from Baiknour, carries two high energy instruments. The soft X-ray instrument on board this mission is eROSITA (**e**xtended **RO**entgen **S**urvey and **I**maging **T**elescope **A**rray), a state of the art X-ray Telescope comprised of seven Wolter-1 telescope modules (TMs). The energy range of eROSITA extends from 0.2 – 8.0 keV. It will create the first all sky survey in the X-ray hard band (2 – 8 keV) and is ∼ 20 times more sensitive than ROSAT in the 0.2 – 2 keV energy range. eROSITA has a field of view with a diameter of 1.03 degrees (Predehl et al. 2021; Merloni et al. 2012).

During the Calibration and Performance Verification phase (CAL-PV), the Abell 3158 cluster was observed as a calibration target on the 21st of November for a duration of 80 ks. The cluster had previously been observed with the *XMM-Newton* observatory. The cluster's appearance is relaxed in the profiles from previous studies making it an excellent candidate to perform a cross-calibration of the two telescopes. The Abell 3158 galaxy cluster is described as being undisturbed in Irwin et al. (1999) and Łokas et al. (2006), however, Hudson et al. (2010) classified the cluster as a non-cool core cluster due to the lack of both bright central core and central temperature drop, while Wang et al. (2010) detected an off-centre cool gas clump to the West of the cluster centre from a two dimensional temperature map. They speculate that the cool gas clump may be present due to a major merger event. The cool gas clump was accompanied with a bow shaped edge and they determined that this cool gas clump is moving adiabatically with this edge. There have also been many estimations of the mass of the cluster with different methods. Moretti et al. (2017) calculated a mass of $1.79 \times 10^{15} M_{\odot}$ using the M_{200} - σ_v relation from Finn et al. (2005). Liu et al. (2020) have estimated the mass from the temperature obtained in X-ray with the M-T relation while Piffaretti et al. (2011) have estimated the mass using the M-L relation. The hydrostatic mass has also been determined eg. (Chen et al. 2007; Eckert et al. 2019). The values for mass obtained with these methods are typically much smaller than those obtained with the velocity dispersions. Additionally, there are a number of extended sources in the A3158 field. They have been observed with X-COP (Eckert et al. 2017) and are not reported about. These extended sources may hold interesting information about the state of the cluster.

In this work we analyse eROSITA CAL-PV data of Abell 3158 and make a comparison to archival *XMM-Newton* and *Chandra* data in which the 1d temperature, abundance and normalisation profiles show good agreement between the telescopes. In §2 the data reduction process is described. In §3 and §4 we describe the imaging and spectral analysis methods and model components. A description of the galaxy velocity dispersion analysis is outlined in §5. We present and discuss our results in §6 with a summary in §7.

The cosmology assumed for the analysis of this paper is ΛCDM with $\Omega_\Lambda = 0.7$, $\Omega_m = 0.3$ and $H_0 = 70$ km s^{-1} Mpc^{-1}. $R_{500} = 1.07$ Mpc is taken from Piffaretti et al. (2011) and using the relation in Reiprich et al. (2013) of $r_{500} \approx 0.65 r_{200}$, r_{200} is calculated to be 1.64 Mpc. At the redshift of the A3158 galaxy cluster, these distances translate to $r_{500} = 15.58$ arcmin and $r_{200} = 23.95$ arcmin, which are the starting values used to determine the extraction radii.

2. Data Reduction

The Abell 3158 Observation ID is 700177 and the processing version used for this work was c001. All seven telescope modules (TMs) were operating nominally for the observation. The telescope was pointed for 80ks to the direction of the cluster. However, during the observation, each TM carried out a filter wheel closed (FWC) observation with a duration of between 10 – 15ks to monitor the particle induced background. Due to this lost observing time, the data with which science can be carried out has an observing time of approximately 60 ks.

The eROSITA data shown here were processed using the eSASS software system developed by the German eROSITA consortium. The eSASS (extended Science Analysis Software System) version that is utilised for the data reduction processes is the eSASSusers_201009 users release from October 2020 (Brunner et al. submitted).

2.1. Filtering Flares

Upon retrieving the data, a flare filtering script was run on the data, a detailed description of which can be found in Reiprich et al. (2021). This was carried out in order to identify any soft proton flares that may have occurred during the observing time. A small number of time bins which have more than 3σ counts remain as these are likely statistical peaks and not real flares. The lightcurve of TM4 shown in Fig. 1 shows the presence of a flare during the time period 37 – 42 ks of the observation followed by the FWC observation. This flare is present after pattern selection and flagging has been applied. The time span of both the flare and the filter wheel closed period are excluded from the GTI of the observation. The lightcurves of the remaining telescope modules are included in the appendix.

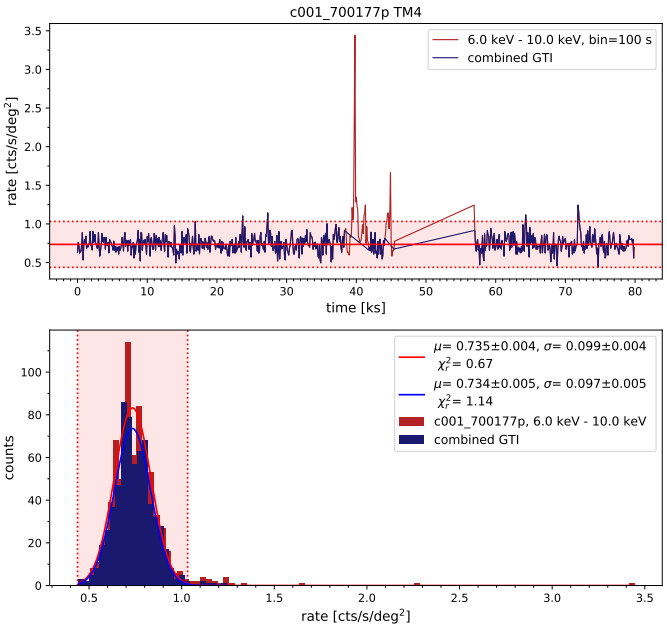

Fig. 1. Lightcurve of TM4 showing a flare excluded from the data.

Following the cleaning of the data from flares, the GTI of the eventlists were updated using `evtool`. The `evtool` task can also be used to merge eventlists. This feature was utilised and a clean merged eventlist was created of TM0, the combination of all seven telescopes. After this, images, exposure maps, and detection masks were created using the eSASS tasks `evtool`, `expmap`

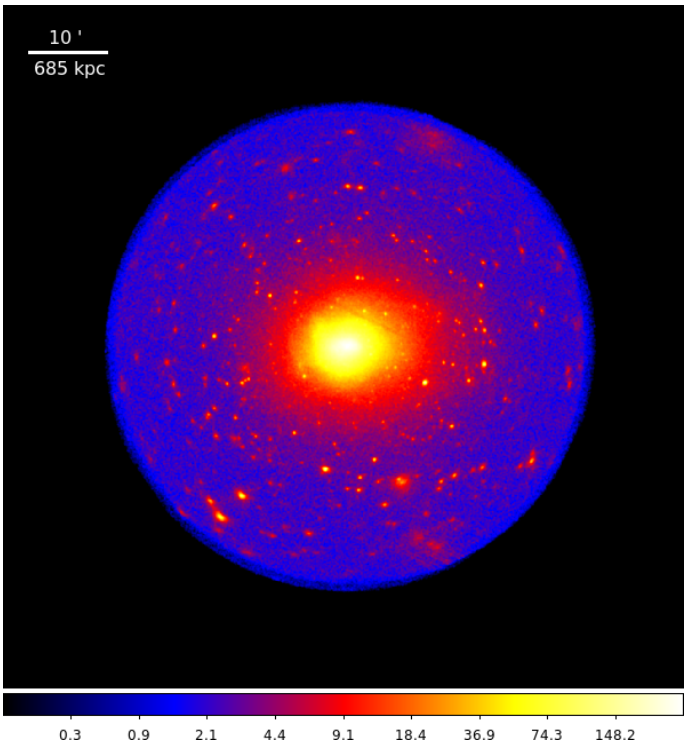

Fig. 2. Smoothed photon image created in the 0.2 – 10 keV energy range using the cleaned TM0 eventlist. TM0 is the combination of all seven telescope modules. The colour bar shows the number of counts.

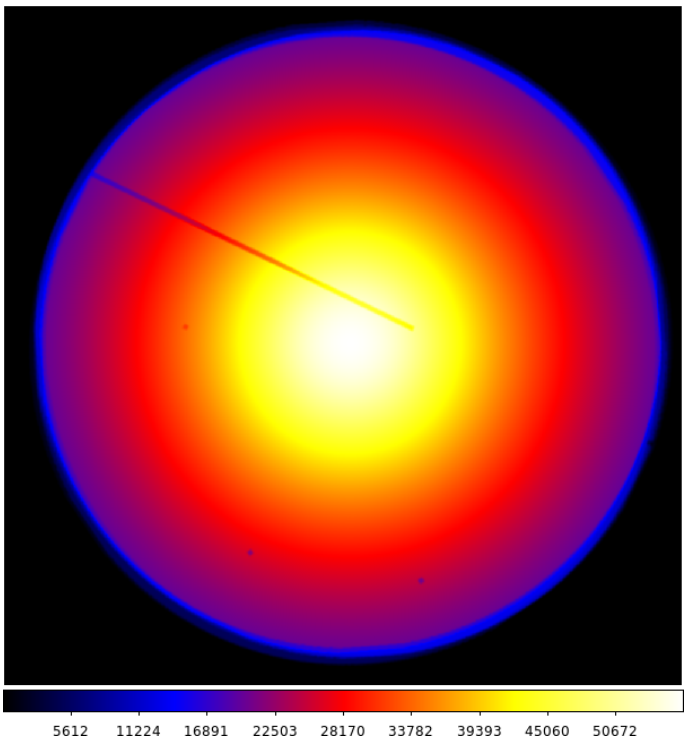

Fig. 3. Exposure map created with the energy range 0.3 – 2.3 keV for TM8 and 1.0 – 2.3 keV for TM9.

and `ermask`, for each telescope and the merged eventlist. The raw TM0 merged image can be seen in Fig. 2. There is an artificial stripe slightly North of the cluster center. This is caused by a column of bad pixels which was removed from TM2. The default exposure map creation does not take into account bad pixels that are identified for the observation. The effect from the removed column in TM2 was propagated to the exposure map which can be seen in Fig. 3. This exposure map was created with the energy range 0.3 – 2.3 keV for TM1, TM2, TM3, TM4, and TM6 (collectively TM8) and with the energy range 1.0 – 2.3 keV for TM5 and TM7 (collectively TM9).

2.2. Source Detection

The `erbox` tool is used to create a rudimentary list of sources present in the observation field of view. A temporary background map is created using `erbackmap` and then `erbox` is run a second time. The resulting list of sources is used as an input for `ermldet` which characterises all sources, it gives information such as the extent and extent likelihood of the sources.

All point sources were masked as well as an extended source to the south of the main cluster which was identified as a cluster from the South Pole Telescope catalogue, SPT-CL J0342-5354 (Bleem et al. 2015). This can be seen in Fig. 4. After the first run of the source detection chain some point sources were missed. Using the adaptive smoothing program from Sanders (2006) a fits image containing smoothing scales for each pixel location is created. The smoothing scale and mask are then used with the adaptive smoothing program to create an image and exposure map with the masked point sources filled in with noise from the surrounding pixels. By dividing the smoothed image by the smoothed exposure map an exposure corrected smoothed image is created. This exposure corrected smoothed image is then multiplied by the original exposure map in order to create a background map which is then used as an input for the erbox and ermldet tasks in order to carry out the source detection. A number of point sources that had not previously been detected were masked after these steps.

2.3. XMM-Newton

Two pointed observations centred on the A3158 galaxy cluster are available on the *XMM-Newton* **S**cience **A**rchive (XSA). The shorter observation is highly contaminated by soft proton flares and so it is excluded from this analysis. There are also four pointings of the outskirts of the cluster, located to the North, West, South, and East of the central pointings. The observation IDs and observing times of each observation is listed in table 1. In order to compare the profiles from eROSITA with *XMM-Newton*, the eventfiles were obtained from the archive to perform analysis on. The analysis carried out in this work closely follows that described in Ramos-Ceja et al. (2019). To summarise, flare filtering was carried out in order to identify and remove any soft proton flares that were present in the observation, CCDs that were in an anomalous state during the observation were removed, and the instrumental background and exposure were corrected for.

Observation Name	Observation ID	Observing Time (s)
Long	0300210201	22392
Short	0300211301	9408
South	0744411501	31000
West	0744411401	33400
North	0744411301	31399
East	0744411601	33800

Table 1. Observation IDs and observing times of the Abell 3158 field with *XMM-Newton*.

Point sources were identified in order to be masked during the spectral extraction process. The central coordinates of the cluster were then determined to be R.A. 55.7108 and Dec. −53.6304 from the emission weighted centre of the *XMM-Newton* central pointing. These central coordinates are used in the analysis of XMM-Newton and eROSITA throughout this paper.

2.4. Chandra

We used *Chandra* observation IDs 3201 and 3712 for the analysis. Both the two observations were taken on ACIS-I. The data reduction was performed using the software `CIAO v4.12`, with the latest version of the *Chandra* Calibration Database (`CALDB v4.9`). Time intervals with a high background level were filtered out by performing a 3σ clipping on the light curve in the 2.3 − 7.3 keV energy range and binned with a time interval of 200 s. The cleaned exposure times were 24.5 ks and 27.3 ks for 3201 and 3712, respectively. Point sources within the ICM were identified with `wavdetect`, and masked after visual inspection. The ancillary response file (ARF) and redistribution matrix file (RMF) were computed using the commands `mkarf` and `mkacisrmf`. Since the emission of A3158 covers the whole CCD area, we extracted and processed the background from the "blank sky" files using the `blanksky` script.

3. Imaging Analysis

3.1. Particle Induced Background (PIB) Subtracted Images

A detailed description of the particle induced background (PIB) subtraction is provided in Reiprich et al. (2021). Using the FWC data, reprojected to the Abell 3158 direction, the same method is used in this work to create a background subtracted image in the 0.3 − 2.3 keV energy band. The process is carried out in the 1 − 2.3 keV energy band for the two telescope modules that do not have an on-chip optical blocking filter (TM5 and TM7). The PIB subtracted photon image is divided by the combined exposure map to create a PIB subtracted count rate image. The product from this process is shown in Fig. 4.

3.2. Surface Brightness Profile

A region file was created with annuli in steps of 10 arcseconds spanning the area from the centre of the cluster to the r_{200}, masking the point sources. With ftools, this region file was used to determine the number of counts in the PIB subtracted photon image which was created in the previous step. The exposure map that was created in this process was also used in order to determine the exposure time in these annuli. An annulus from r_{200} out to 31.00 arcmin, was determined as the sky background region and the number of counts and the exposure time in this region were extracted using the same method as described above.

The surface brightness for each annulus was calculated by dividing the counts by the exposure and the area and subtracting surface brightness of the background region. This surface brightness was then plotted as a function of distance from the centre of the cluster. The surface brightness profile is shown in Fig. 5. The error bars shown in the profile are determined from the PIB-subtracted photon image, the exposure map and the sky background. These errors are propagated through the calculations and are taken into account when determining the final value of the surface brightness of each region.

A surface brightness profile was created using the *XMM-Newton* data in the same method as described above. The sky background is determined from the background spectral fitting region in the four outer pointings.

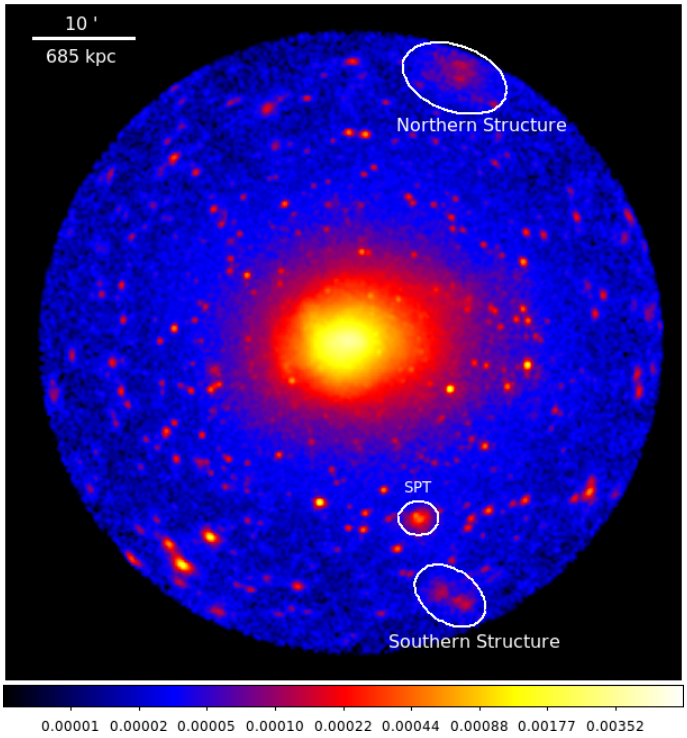

Fig. 4. Particle induced background subtracted count rate image in the 0.3 − 2.3 keV energy band. The extended source to the south of the cluster was identified as the SPT cluster.

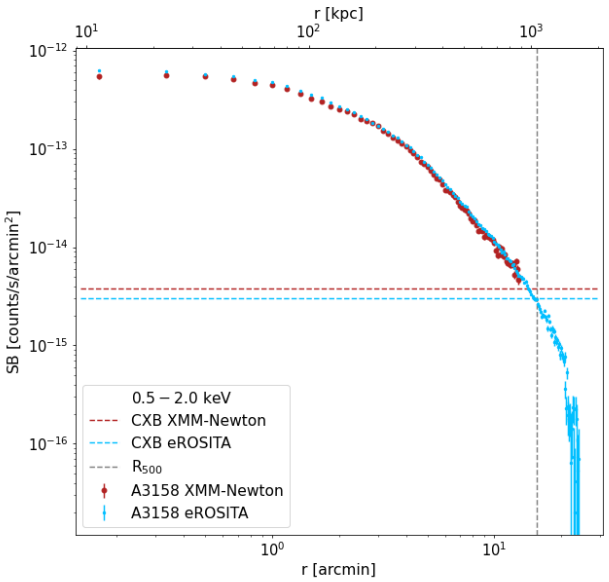

Fig. 5. Comparison of the surface brightness profile from XMM-Newton out to r_{500} and from eROSITA out to r_{200}. The data points are PIB subtracted and sky background subtracted

4. Spectral Analysis

4.1. Profiles

Using the `srctool` task in eSASS, cluster and background spectra were extracted. The cluster spectrum was obtained within r_{200} centred at the location R.A. 55.7108°, and Dec. −53.6304°. The background spectra are extracted from an annulus centred around the cluster with a width of 7.05 arcmin, i.e. from 23.95(r_{200}) − 31.0 arcmin. The `srctool` task also extracts the necessary files to perform spectral fitting, such as the Auxiliary Response File (ARF) and the Redistribution Matrix File (RMF). These spectra were then grouped with a minimum of 5 counts in each channel.

Additionally the FWC data were reprojected and spectra, ARF, and RMF files were extracted using the full field of view and a region excluding a circle in the centre with a radius of 5 arcmin. The latter was used to renormalise the FWC data based on the hardband count rate in source and FWC data.

For all of the spectral fitting carried out in this paper, the `XSPEC` software package (Arnaud 1996) was used. The X-ray background was modelled with an unabsorbed 0.099 keV thermal *apec* (Smith et al. 2001) component to model the Local Hot Bubble (LHB) emission, an absorbed 0.22 keV thermal *apec* component to model the Milky Way Halo (MWH) (McCammon et al. 2002) emission and an absorbed powerlaw component with a photon index of 1.41 (De Luca & Molendi 2004) to model the unresolved Active Galactic Nuclei (AGN) emission. The `tbabs` absorption model (Wilms et al. 2000) was used throughout the work. As there is likely some residual cluster emission located outside r_{200}, an absorbed thermal *apec* component is included in the background model to account for the cluster emission. The quiescent particle background was handled by `XSPEC` by loading the FWC data as background for each dataset. The statistics used in the fitting process was the Poisson distributed C-statistic(Cash 1979). In order to ensure that these results are robust, the data was fit with Gaussian distributed chi-squared statistics with a minimum grouping of 100 counts in each channel. The results obtained using the two methods were very similar and so the c-statistic was used for the analysis. The value for the galactic hydrogen column density, n_H, is 1.4×10^{20} cm^{-2} which is taken from the UK Swift Science Data Centre[1] which is calculated based on Willingale et al. (2013). The abundance table that was used for this work was the one provided in Lodders (2003). The redshift value of $z = 0.059$ was taken from Struble & Rood (1999). The values for the abundance and redshift of the background components were frozen to $Z = 1.0\ Z_\odot$ and $z = 0.0$. The redshift of the cluster was frozen to $z = 0.059$ and the n_H was frozen to $n_H = 1.4 \times 10^{20}$ atoms cm^{-2}. The temperature, abundance and normalisation for the cluster, along with the background normalisations, were varied while the model was fit. The fit was carried out in the 0.5 – 9.0 keV energy range for telescope modules with an on-chip filter while the fit for the telescope modules without an on-chip filter was carried out in the 0.8 – 9.0 keV energy range. The resulting values were plotted as a function of distance from the cluster centre.

4.2. XMM-Newton

The spectral extraction of the source spectra was carried out just with the central pointed observation of A3158 and the sky background spectra were extracted between 23.95(r_{200}) – 31.00 arcmin from four surrounding pointed observations that were part of the ***XMM-Newton*** **C**luster **O**utskirts **P**roject (X-COP) Eckert et al. (2017). The spectra were fit with the same model as described in Ramos-Ceja et al. (2019). This model is similar to the model fit to the eROSITA spectra with the inclusion of a number of instrumental lines and Chi-squared statistics were used in the fitting process. The fit was carried out in the 0.5 – 9.0 keV energy range excluding the energies in the 0.9 – 1.3 keV energy range where the Fe L line can be found.

4.3. Chandra

Limited by the field of view (FoV), we only obtained the profiles within 9 arcmin. The center of the profiles was set at (R.A.=55.7246, Dec.= -53.6353). The spectra were fitted with `Xspec 12.11.1` (Arnaud 1996) adopting C-statistic (Cash 1979) and the solar abundance table from Lodders (2003). Galactic hydrogen absorption was modeled by `tbabs` (Wilms et al. 2000), where the Galactic hydrogen column density $n_{\rm H}$ was fixed at 1.4×10^{20} cm^{-2}. The full band (0.5–7 keV) spectrum was fitted with a single `apec` thermal plasma emission model (Smith et al. 2001). The redshift was fixed at 0.059, while the temperature, metal abundance, and normalisation were set as free parameters.

4.4. Temperature Map

Wang et al. (2010) performed a thorough X-ray analysis of the Abell 3158 galaxy cluster with *XMM-Newton* and *Chandra* observations. A two dimensional temperature map of the cluster was created and the presence of an off-centre cool gas clump was highlighted in the paper. Additionally, though the surface brightness profile of the cluster appears regular, it does not host a cool core as relaxed clusters are typically expected to have. Due to this previously discovered substructure and the apparent lack of a cool core we decided to create a temperature map with the new eROSITA data. The contour binning package from Sanders (2006) was utilised in this process.

The annulus of the region from which the background spectra were extracted extended from 23.95(r_{200})−31.00 arcmin. This region was excluded from the creation of the binmap. Two masks were created to be used as input into the contour binning script from Sanders (2006). The first mask created excluded the observation outside r_{500} and the second mask excluded the observation inside r_{500} and outside r_{200}. A signal to noise ratio of 150, constrain value of 1.5, and a smoothing signal to noise ratio of 50 were implemented on the first mask. A signal to noise ratio of 200 was implemented on the second mask. The two resulting binmaps were merged to create one final binmap with larger bins in the outer radius.

An extraction code which utilised the `srctool` task from eSASS was implemented. This code took the binmap and a weight image as inputs and created for each bin, a mask and a weighted mask. This mask is used as the input for `srctool` and the spectra, ARF and RMF were extracted. Once spectra were extracted, the FWC data was renormalised and the spectra were grouped with minimum 25 counts in each bin.

The fitting script which was designed for use with *XMM-Newton* data was adapted for use with the eROSITA binmap and spectra using the same energy range as previously but switching to Chi-squared statistics. This change in statistics does not have a large impact on the results as the tests run on the profiles had shown. Firstly the fit was carried out with the abundance fixed at 0.3, after this the abundance was varied and the fit was run again.

[1] https://www.swift.ac.uk/analysis/nhtot/index.php

The products of the script are a temperature map with fixed abundance, a temperature map with free abundance and an abundance map. Bins that had values of temperature larger than 30.0 keV, a reduced chi-squared value for the fit greater that 1.5 or a relative error value greater than 50% were not included in the temperature map with fixed abundance. The same criteria were used for the temperature map with varying abundance with added criteria being rejecting abundance values where the maximum error value is less than the measured value. The temperature map with free abundance is shown in §6.

4.5. Mass-Temperature Relation

Using an annulus extending from $0.2 - 0.5\ r_{500}$, the spectra were extracted and the temperature in this region was determined following the fitting model described above. The temperature measured in this region was 4.725 ± 0.035 keV. From this measurement of the temperature T_{500}, the M-T scaling relation

$$\log\left(\frac{M_{500}}{C_1}\right) = a \cdot \log\left(\frac{T_{500}}{C_2}\right) + b$$

from Lovisari et al. (2015) was used to get an estimate of the cluster mass where $C_1 = 5 \times 10^{13} h_{70}^{-1} M_\odot$ and $C_2 = 2$ keV are constants of the scaling relation and $a = 1.62 \pm 0.08$ and $b = 0.24 \pm 0.04$ are the fit results of the scaling relation for HIFLUGCS cluster with a temperature $kT > 3$ keV. The mass value determined was $M_{500} = 3.50 \pm 0.40 \times 10^{14} M_\odot$. The uncertainties of the scaling relation have been propagated here. A value for the r_{500} was then estimated to be 1.05 ± 0.04 Mpc from the relation described in Reiprich et al. (2013). The relation between r_{500} and r_{200} of $r_{500} \approx 0.65 r_{200}$, which assumes an NFW (Navarro et al. 1997) profile with concentration $c = r_{200}/r_s = 4$ is then used to get an estimation of M_{200} which is calculated to be $M_{200} = 5.09 \pm 0.59 \times 10^{14} M_\odot$. This value for the mass will be compared to the mass determined with a M_{200} - σ_v relation in §6.4.

5. Member Galaxies Velocity Distribution

From the OmegaWINGS galaxy spectroscopy survey (Moretti et al. 2017), member galaxies in the Abell 3158 field were identified and compiled into a list consisting of 213 member galaxies. This survey determined the membership of galaxies in the field by using a redshift cut of $0.05 < z < 0.07$, a magnitude cut of 20 mag in the V filter and a spatial limitation of the galaxies within 30 arcmin of the cluster.

Implementing the same cuts on a search using the NASA/IPAC Extragalactic Database (NED)[2], an additional 152 galaxies were identified as members of the Abell 3158 cluster after filtering any galaxies that had already been identified in the OmegaWINGS survey (Moretti et al. 2017). The filtering was carried out by cross checking the right ascension, declination and redshift values of each galaxy. This list contains positions and spectroscopic redshifts from surveys such as Havlen & Quintana (1978), Quintana & Ramirez (1995), Katgert et al. (1998), Smith et al. (2004), Cava et al. (2009) and Moretti et al. (2017).

Adding the two lists of galaxies gives a total number of 365 member galaxies within 30 arcmin of the cluster with redshifts $0.05 < z < 0.07$. Using the redshift measurements, a rudimentary velocity is calculated using $v = cz$, where c is the speed of light in a vacuum, and a histogram of the galaxy velocities

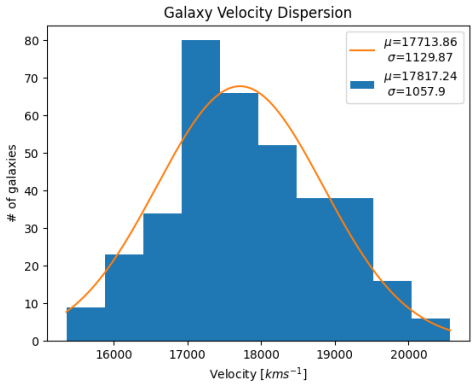

Fig. 6. Histogram of member galaxy velocities with a redshift range of $0.05 < z < 0.07$. The orange curve is the best fit Gaussian of the data set.

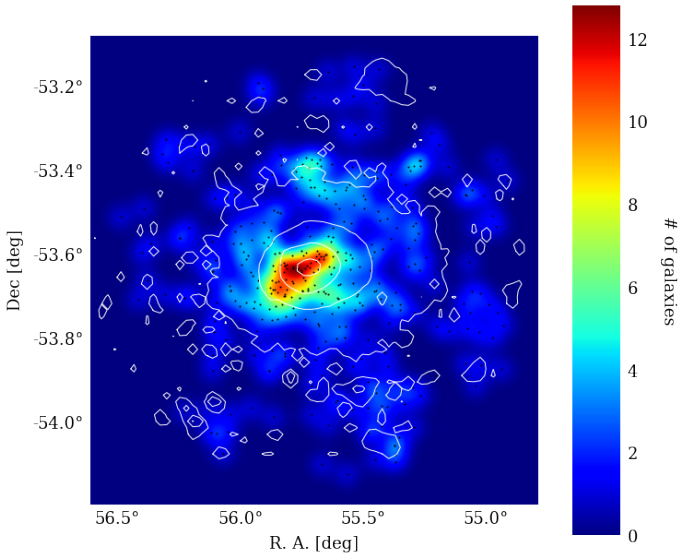

Fig. 7. Galaxy density map with members of Abell 3158. The extended source in the south of field coincides with a small overdensity of galaxies, the location of which can be seen in Fig. 4. These galaxies have redshifts in the range $0.05 < z < 0.07$.

was plotted, Fig. 6. From this histogram the standard deviation of the data set of 1058 ± 41 kms^{-1} is determined to be the velocity dispersion of the cluster member galaxies. The errors on the redshifts were obtained from Moretti et al. (2017) and from NED and from these the errors on the velocities were calculated. The error of the velocity dispersion was determined to be the standard deviation of the error values of the velocities.

Along with the histogram of galaxy velocities, using the positions of the member galaxies, a density map of the list of member galaxies was created with X-ray contours from eROSITA overlaid, seen in Fig. 7.

The velocity dispersion measured can then be used to determine the cluster mass. Moretti et al. (2017) makes use of a M_{200} - σ_v relation from Finn et al. (2005). With a σ_v value of 1023 kms^{-1} they calculate $M_{200,c}$ as $1.79 \times 10^{15} M_\odot$.

Using the same method, the $M_{200,c}$ is determined with the velocity dispersion determined in this work (1058 ± 41 kms^{-1}). The mass is calculated to be $1.98 \pm 0.23 \times 10^{15} M_\odot$ with the errors determined by Gaussian error propagation. The value of the mass determined in this paper is consistent with Moretti et al. (2017).

[2] http://ned.ipac.caltech.edu/

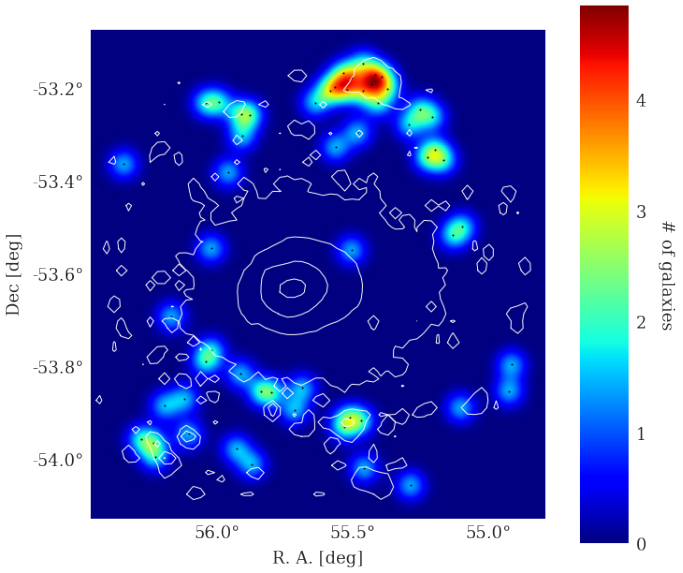

Fig. 8. Galaxy density map of member 2 galaxies classed as probable separate substructure. These galaxies have a redshift in the range $0.070 < z < 0.077$. X-ray contours are overlaid showing that the extended source in the North is located in the same region as the overdensity of galaxies.

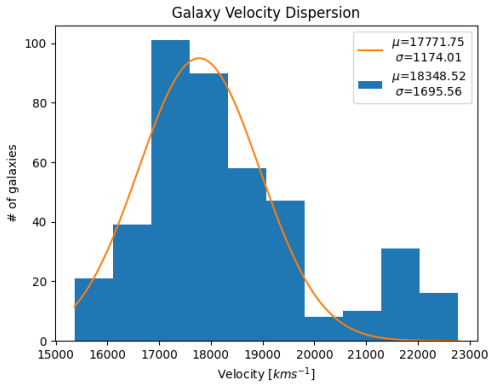

Fig. 9. Histogram of galaxy velocities with members of A3158 and members of a separate substructure. The substructure can be seen as an increased population of velocities to the right of the initial peak. The orange curve is the best fit Gaussian to the data set.

Implementing an updated $M_{200} - \sigma_v$ relation from Bocquet et al. (2015) with the velocity dispersion from both this work and Moretti et al. (2017) results in $M_{200,c}$ values of $1.38 \pm 0.25 \times 10^{15} M_\odot$ and $1.23 \pm 0.19 \times 10^{15} M_\odot$ respectively. This shows that this work is in agreement with Moretti et al. (2017), as expected given the consistent velocity dispersion, though the $M_{200,c} - \sigma_v$ relations from Finn et al. (2005) and Bocquet et al. (2015) are not consistent.

In the OmegaWINGS survey there are a number of galaxies that have been identified as probable members of substructure. These galaxies all have a redshift value in the range $0.070 < z < 0.077$. Galaxies with the same redshift range from the NED search were added to the OmegaWINGS list. A galaxy density map was plotted with the positions of these galaxies and is shown in 8.

Combining the list of members of A3158 and the list of members of substructures a histogram of the velocities was plotted and is shown in Fig. 9.

5.1. Serendipitous Extended Sources

There are three extended sources observed serendipitously in the Abell 3158 pointed observation. Two of these are located to the South of the cluster and one is located to the North/North-West of the cluster. The extended source that is closest to the cluster centre in the South of the field of view was identified as a ~ 0.5 redshift cluster that has previously been observed by the **S**outh **P**ole **T**elescope (SPT) survey Bleem et al. (2015), SPT-CL J0342-5354.

While this cluster is detected with very high significance in the eROSITA observation, the number of source photons is insufficient for a detailed spectroscopic analysis that could constrain an X-ray redshift. There are also no galaxies with a spectroscopic redshift close to that of the cluster observed in the optical band. In Fig. 8, it appears that an overdensity of galaxies in the redshift range $0.070 < z < 0.077$ coincides with an X-ray overdensity with the same location as the SPT-CL J0342-5354 cluster. We speculate that this is a coincidence.

The two remaining extended sources in the field of view have not been documented previously. As the sources are at the edge of the field of view, the count rates are low and spectral analysis is not possible. However, as can be seen in the galaxy density maps in §5, there are overdensities of galaxies overlapping with the X-ray overdensities. The locations of these extended sources are listed in table 2.

Location	R.A.	Dec.	Redshift range
North	55.4216	-53.1991	0.070 - 0.077
South	55.3949	-54.0638	0.05 - 0.07

Table 2. Right Ascension and Declination of the extended sources detected in the North and the South of the FoV.

6. Results and Discussions

6.1. 1D Profiles

Following the steps outlined in §4.1, the temperature, abundance and normalisation profiles of A3158 are extracted and shown in Fig. 10. Looking first at the temperature profile it is clear that the measurement from all three telescopes shows that the cluster does not have a cool core. The results from eROSITA are ~ 0.5 keV lower than the results from *Chandra* in the central region and overall slightly higher than *XMM-Newton* results out to r_{500}. Though the telescopes are not in agreement with each other, the shape the temperature profile follows is similar. The shape is also in agreement with the published *Chandra* central temperature profile (Hudson et al. 2010, their Fig. 2). In the abundance profile, the outer two annuli for the *XMM-Newton* observation are frozen at $Z = 0.3\ Z_\odot$ as during the fitting these values were estimated to be very low and the temperature and normalisation results were affected. The low photon count in the outskirts of the *XMM-Newton* central pointing field of view, likely has an impact on this issue. This issue is resolved with eROSITA and abundance measurements past r_{500} are possible with good constraints. The normalisation values of the eROSITA telescope are lower than the *XMM-Newton* measurements over the full field of view with the exception of the central bin. This is clear to see in the ratio plot shown in Fig. 11.

Comparing the results from X-COP (Eckert et al. 2017) and the *XMM-Newton* analysis performed in this work there is agreement in the central regions on a $\sim$ 10% level and agreement

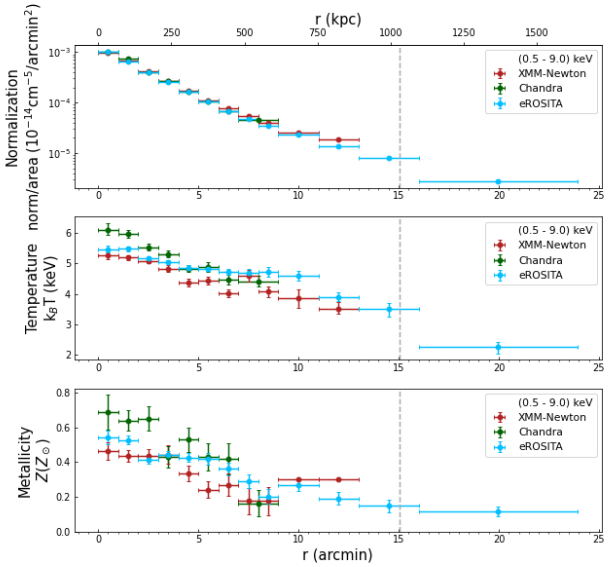

Fig. 10. Normalisation, temperature and metal abundance profiles showing the comparison of eROSITA to *XMM-Newton* and *Chandra*. The grey dashed line represents the r_{500} of the cluster.

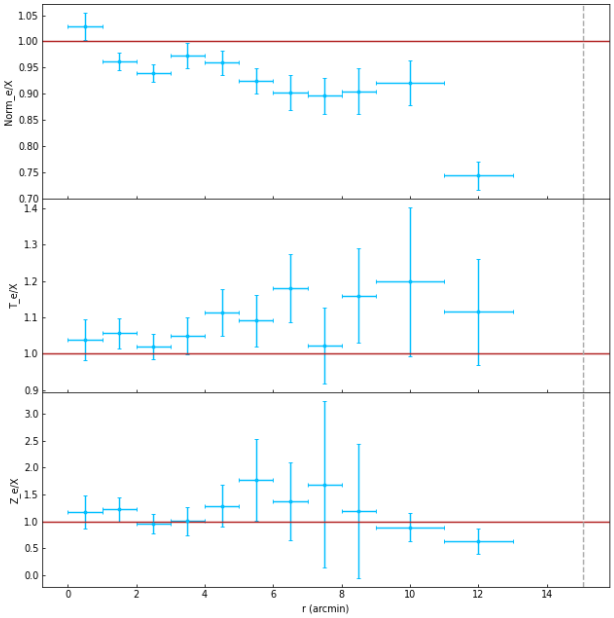

Fig. 11. Plot of the normalisation, temperature and abundance ratios of eROSITA/*XMM-Newton*. The grey dashed vertical line is the r_{500} of the cluster.

in the outer regions on a $\sim$ 20% level. The larger difference in the outer regions is not surprising as our analysis of the XMM-Newton data uses the X-COP pointings only for the background determination while Eckert et al. (2017) use these pointings to determine both the background and the profiles out to larger radii.

Also clear from the ratio plot in Fig. 11 is that the normalisation, temperature and abundance profiles generally agree on a $\lesssim$ 10% level. This is also true for the comparison between eROSITA and *Chandra*, the ratio plot of which can be found in the appendix. This is an acceptable level of agreement when compared to the other satellites so shortly after the beginning of eROSITA operations. Moreover, the presence of multitemperature structure in the ICM as observed in the temperature map may contribute to differences between X-ray telescopes. Fitting the spectra with a single-temperature model can lead to a dependency on the observing telescope, although naively we would expect the opposite trend in temperature (e.g., Fig. 18 in Reiprich et al. 2013).

The sensitivity of the instrument at low energies can have an impact on the weighting of the Fe L shell emission line complex. As the *XMM-Newton* analysis excludes the energy range where the Fe L shell emission line is located, the results are not likely to fully agree with those determined with eROSITA, although also this might naively lead to the opposite trend. Additionally, the discrepancy between *XMM-Newton* and *Chandra* has been previously documented in Schellenberger et al. (2015) (quantitatively confirmed again in Migkas et al. 2020, their Fig. A.8) to arise from the systematic effective area calibration uncertainties, and so the difference observed between the results from these two telescopes is not surprising.

Overall, since the eROSITA telescope has a larger field of view than both *XMM-Newton* and *Chandra*, we can extract the profiles out to larger radii and deliver good measurements and constraints for example in the abundance profile.

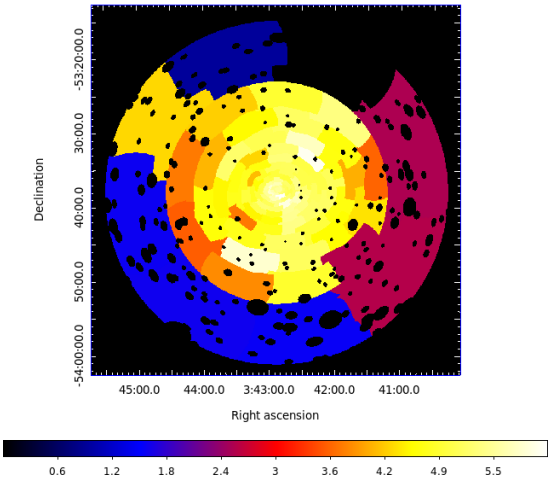

Fig. 12. Temperature map of Abell 3158 from eROSITA. The SPT cluster has been masked. The colour bar represents the temperature in keV.

6.2. Temperature Map

The temperature map that was created using the steps in 4.4 is shown in Fig. 12. Immediately clear from this temperature map is more indication that the cluster does not have a cool core as would be expected in a regular looking cluster such as this. Wang et al. (2010) also produced a temperature map using the *XMM-Newton* observation of the cluster which is seen in Fig. 14. There is an evident cool region detected in the west of this image. In order to make a comparison with the *XMM-Newton* and eROSITA data, a second image of the temperature map was generated with the same dimensions and scale as Wang et al. (2010). This is shown in Fig. 15. The location of the cool region is also detected in the eROSITA temperature map. Not only does the location of the cool clump agree but the presence of the sharp

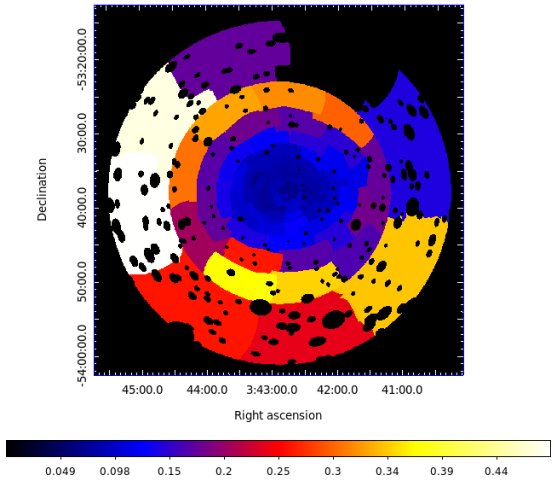

Fig. 13. Relative error map corresponding to figure 12.

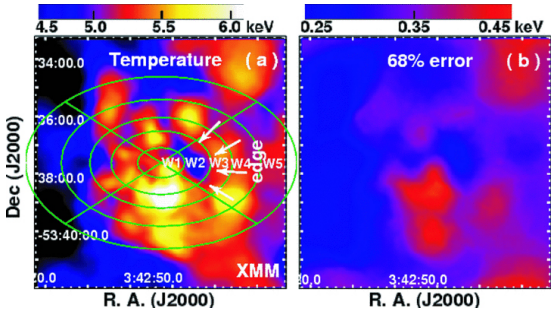

Fig. 14. Temperature and error map from Wang et al. (2010).

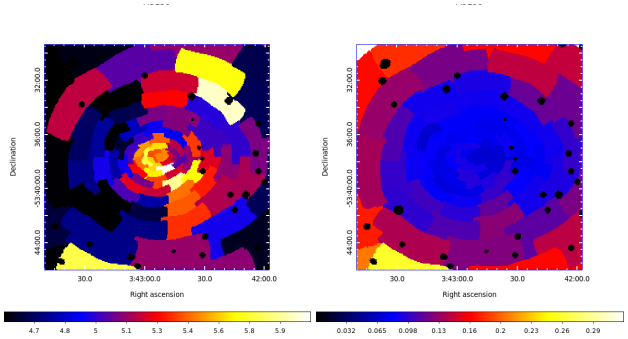

Fig. 15. The temperature map created using eROSITA data in the same coordinate dimensions as Wang et al. (2010). The values of the error calculated with eROSITA are much smaller than those for *XMM-Newton*.

increase in temperature to the West of this feature is also present in both maps. The East of the cluster hosts lower temperatures in the range 3.5 – 5.0 keV in both maps as well as increased temperature to the North and South of the central region. 5.5 – 6 keV gas is detected ∼ 6 – 7 arcmin in the North West direction in both maps. The error map created from eROSITA shows significantly lower error values to the *XMM-Newton* error map.

The lack of a cool core and the presence of the off-centre cool clump in both the *XMM-Newton* and eROSITA temperature maps suggests that the Abell 3158 cluster is not in a relaxed state. There may be some merger activity ongoing in the cluster. The elongation of the overall X-ray surface brightness distribution in East-West direction would be consistent with a merger-induced sloshing scenario in this direction.

6.3. Velocity Distribution

From the galaxy density maps, it is clear that X-ray overdensities coincide with overdensities of galaxies. In the North of the field, there is a population of galaxies that are classed as a probable separate substructure. This substructure corresponds with the extended source that is detected in the north of the cluster in both eROSITA and *XMM-Newton*. The galaxies in this region are in the redshift range $0.070 < z < 0.077$.

In the South of field there is also an overdensity of galaxies that are classed as members of the A3158 cluster. This overdensity coincides with the location of both the SPT cluster and the Southern extended source. This population of galaxies may be a substructure of A3158 that happens to be located at the same position as the SPT cluster. It it possible that the Abell 3158 cluster is undergoing merger activity and that the substructure in the South of the FoV is being accreted by the cluster.

6.4. Mass Determination

As discussed in §4, the mass of the cluster was estimated from the M-T relation (Lovisari et al. 2015). The M_{500} was estimated to be $3.50 \pm 0.40 \times 10^{14}$ $M_{\odot}$. This is not consistent with the value determined by Liu et al. (2020) of $M_{500} = 4.53 \pm 0.11 \times 10^{14}$ $M_{\odot}$ which was determined using the same method. However, Liu et al. (2020) utilised *Chandra* data to determine the mass from the M-T relation. Schellenberger et al. (2015) show that the temperature measurements from *Chandra* are higher than those from *XMM-Newton* and as shown in this work, the eROSITA telescope temperature measurements are also lower than the *Chandra* results. This may explain the discrepancy between these results. The hydrostatic mass was also determined in Eckert et al. (2019) and was determined to be $M_{500} = 4.26 \pm 0.18 \times 10^{14} M_{\odot}$. Converting to M_{200}, the mass estimated for A3158 from this work was $M_{200} = 5.09 \pm 0.59 \times 10^{14} M_{\odot}$. This is not in agreement with the hydrostatic mass value determined in Eckert et al. (2019) of $M_{200} = 6.63 \pm 0.39 \times 10^{14} M_{\odot}$.

In §5 the mass of the cluster was calculated using the mass - velocity dispersion (M-σ_v) relation. The velocity dispersion determined in both this work and Moretti et al. (2017) are consistent with each other leading to consistent mass measurements. The Bocquet et al. (2015) M-σ_v relation is used to calculate a value for $M_{200,c}$ of $1.38 \pm 0.25 \times 10^{15} M_{\odot}$ with a velocity dispersion of 1058 ± 41 kms^{-1}. Implementing the same $M_{200,c} - \sigma_v$ relation with the velocity dispersion from Moretti et al. (2017) a mass value of $1.23 \pm 0.19 \times 10^{14} M_{\odot}$.

In dynamically active clusters it is possible that the velocity dispersion can be biased high. As we have indicated that A3158 may be undergoing some merger activity, the velocity dispersion could be biased high. This would have a knock on effect of causing the mass estimate to also be biased high.

Furthermore, it has been found that the observed temperature in merging clusters can be biased low relative to the total mass of the system because it takes time for the kinetic energy released during the merger to become completely thermalised (e.g., Kravtsov et al. 2006). This can influence the mass estimate from the M-T relation to also have a low bias. A summary of the comparison of the results is shown in table 3.

Taking these factors into account, it is possible that the true M_{200} of A3158 lies between $5.09 \times 10^{14} - 13.8 \times 10^{14} M_{\odot}$.

Publication	Method	Mass	Result ($10^{14} M_\odot$)
This work	M-T	M_{500}	3.5 ± 0.40
Liu et al.	M-T	M_{500}	4.53 ± 0.11
X-COP	Hydrostatic	M_{500}	4.26 ± 0.18
This work	M-T	M_{200}	5.09 ± 0.59
X-COP	Hydrostatic	M_{200}	6.63 ± 0.39
This work	M-σ_v, Bocquet	M_{200}	13.8 ± 2.5
Moretti et al.*	M-σ_v, Bocquet	M_{200}	12.3 ± 1.9
This work	M-σ_v, Finn	M_{200}	19.8 ± 2.3
Moretti et al.	M-σ_v, Finn	M_{200}	17.9

Table 3. Summary of the masses determined in this work and the literature values they are compared to. *Though Moretti et al. (2017) did not compute the mass using the Bocquet et al. (2015) relation, the σ_v value they calculated was used with this relation in this work for the purpose of the comparison. Eckert et al. (2019) is listed as X-COP.

6.5. Cluster Morphology

The PIB subtracted background image is shown again in Fig. 16. The image on top, in linear scale, is zoomed in to the central region of the cluster. The bow shaped edge to the West of the emission peak is close to where the cool gas clump discussed in 6.2 is located. This has been observed by Wang et al. (2010) where they have determined that the cool gas clump is moving adiabatically behind this bow shaped edge which was determined to be a faint cold front. This edge exists approximately ~ 2 arcmin (~ 137 kpc) from the cluster centre.

Additionally, there exists an extension of gas ~ 10 arcmin (~ 865 kpc) to the West of the cluster centre, observed in the bottom image in the logarithmic scale. We present this extension of gas as a new finding. The irregularities between the different scales would suggest that there may be a sloshing effect occurring in the cluster further supporting the claim that the cluster is undergoing merger activity.

7. Conclusions

The Abell 3158 galaxy cluster was observed by the eROSITA observatory as a calibration source. A comparison of the 1 dimensional temperature, metal abundance and normalisation profiles between the eROSITA observation and archival *XMM-Newton* and *Chandra* data was carried out. The temperatures measured with eROSITA, *XMM-Newton* and *Chandra* agree on a $\lesssim 10\%$ level and the profiles trend in the same direction showing that the cluster lacks a cool core. The metal abundance profile of the three telescopes shows a definitive decrease with increase in radius as is expected and also agrees on a $\lesssim 10\%$ level. The eROSITA telescope provides tighter constraints on the metal abundance out to large radii. The normalisation profile shows that the values obtained from the *XMM-Newton* observation are higher than the those from the eROSITA observation but are also within $\lesssim 10\%$. The normalisation values from *Chandra* are in good agreement with the eROSITA data.

There are a large number of galaxies with spectroscopic redshifts in the Abell 3158 field. A redshift cut of $0.05 < z < 0.07$ was implemented for the determination of cluster members and the velocity of these redshifts were calculated. The velocity dispersion of the member galaxies was determined and a value for $M_{200,c}$ of $1.38 \pm 0.25 \times 10^{15} M_\odot$ was calculated using the mass - velocity dispersion relation. Using the M-T relation the M_{200} is determined to be $5.09 \pm 0.59 \times 10^{14} M_\odot$. Since dynamically active clusters typically have a velocity dispersion that is biased high and clusters undergoing merger activity host temperatures that are biased low, the true value of the cluster mass may lie between these values. The disagreement between the mass estimates further supports the claims that the cluster is undergoing merger activity.

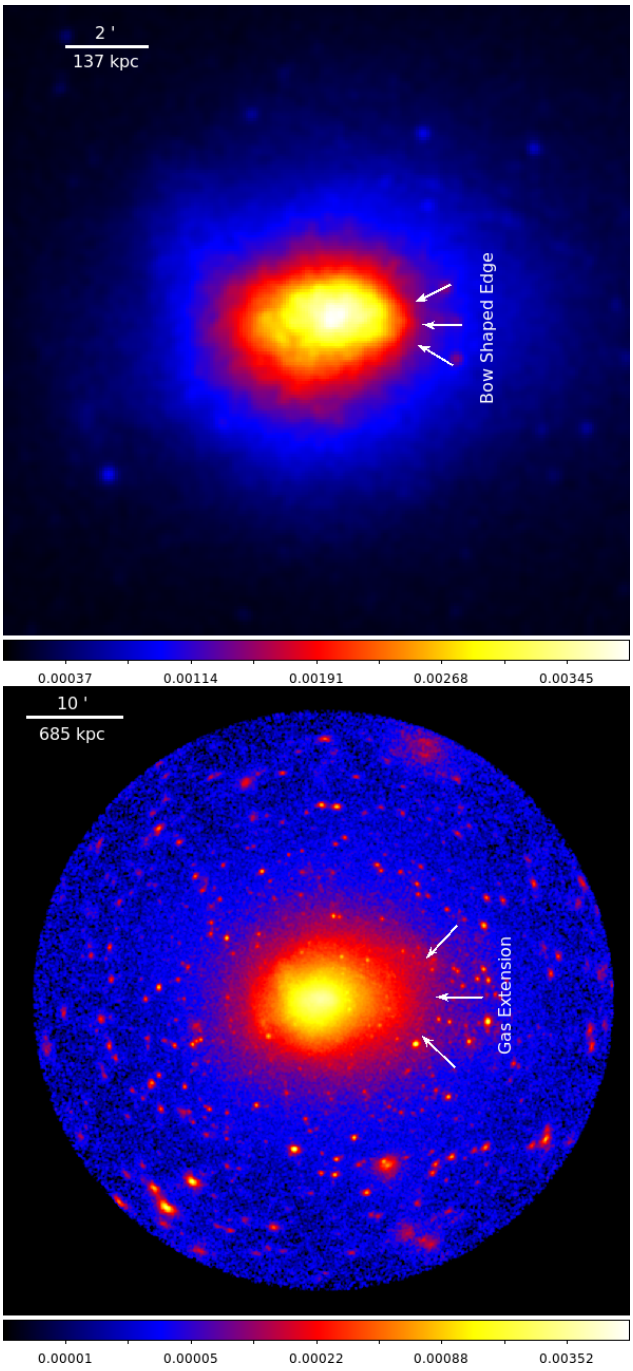

Fig. 16. Top: PIB subtracted count rate image in linear scale, zoomed in to the central region to show the Bow shaped edge. Bottom: PIB subtracted count rate image in logarithmic scale with arrows showing the large extension of gas to the West of the cluster. Both images are smoothed.

A population of galaxies with a spectroscopic redshift range $0.070 < z < 0.077$ was identified as a probable separate structure which corresponds to an extended source in the North of the field of view. A similar extended source detected 1.85 Mpc south of the main cluster also hosts an overdensity of galaxies. The galaxies located in the Southern extended source are located

at the same redshift as the main galaxy cluster. It is, therefore, likely being accreted onto the A1358 cluster. A high redshift cluster previously discovered by SPT is also detected South of the cluster centre.

The 2 dimensional temperature map of the cluster showed that the cluster does not have a cool core. In fact there is a cool clump in the west of the central region which has been observed before. This matches closely the temperature map presented in Wang et al. (2010). The off-centre cool clump and the lack of a cool core suggests that the cluster is not relaxed and may be undergoing some merger activity. The detection of a bow shaped edge $\sim$ 137 kpc located near the cool gas clump to the West of the cluster centre found in this work is also consistent with the previously discovered cold front with the *XMM-Newton* and *Chandra* observations. An extension of gas $\sim$ 685 kpc West of the cluster centre is a new discovery and supports the idea that the cluster is not relaxed but is undergoing merger activity. Together the surface brightness and temperature map analyses clearly confirm that this is a disturbed cluster.

Acknowledgements. This work is based on data from eROSITA, the soft X-ray instrument aboard SRG, a joint Russian-German science mission supported by the Russian Space Agency (Roskosmos), in the interests of the Russian Academy of Sciences represented by its Space Research Institute (IKI), and the Deutsches Zentrum für Luft- und Raumfahrt (DLR). The SRG spacecraft was built by Lavochkin Association (NPOL) and its subcontractors, and is operated by NPOL with support from the Max Planck Institute for Extraterrestrial Physics (MPE). The development and construction of the eROSITA X-ray instrument was led by MPE, with contributions from the Dr. Karl Remeis Observatory Bamberg & ECAP (FAU Erlangen-Nuernberg), the University of Hamburg Observatory, the Leibniz Institute for Astrophysics Potsdam (AIP), and the Institute for Astronomy and Astrophysics of the University of Tübingen, with the support of DLR and the Max Planck Society. The Argelander Institute for Astronomy of the University of Bonn and the Ludwig Maximilians Universität Munich also participated in the science preparation for eROSITA. The eROSITA data shown here were processed using the eSASS software system developed by the German eROSITA consortium. Part of this work has been funded by the Deutsche Forschungsgemeinschaft (DFG, German Research Foundation) – 450861021. This work was supported in part by the Fund for the Promotion of Joint International Research, JSPS KAKENHI Grant Number 16KK0101. This research has made use of the NASA/IPAC Extragalactic Database (NED), which is funded by the National Aeronautics and Space Administration and operated by the California Institute of Technology. This research has made use of the VizieR catalogue access tool, CDS, Strasbourg, France (DOI: 10.26093/cds/vizier). The original description of the VizieR service was published in A&AS 143, 23 We would like to express thanks to Professor Haiguang Xu for allowing us to show the temperature map created using *XMM-Newton* published in Wang et al. 2010.

References

Arnaud, K. A. 1996, in Astronomical Society of the Pacific Conference Series, Vol. 101, Astronomical Data Analysis Software and Systems V, ed. G. H. Jacoby & J. Barnes, 17
Bleem, L. E., Stalder, B., de Haan, T., et al. 2015, ApJS, 216, 27
Bocquet, S., Saro, A., Mohr, J. J., et al. 2015, ApJ, 799, 214
Cash, W. 1979, ApJ, 228, 939
Cava, A., Bettoni, D., Poggianti, B. M., et al. 2009, A&A, 495, 707
Chen, Y., Reiprich, T. H., Böhringer, H., Ikebe, Y., & Zhang, Y. Y. 2007, A&A, 466, 805
De Luca, A. & Molendi, S. 2004, A&A, 419, 837
Eckert, D., Ettori, S., Pointecouteau, E., et al. 2017, Astronomische Nachrichten, 338, 293
Eckert, D., Ghirardini, V., Ettori, S., et al. 2019, A&A, 621, A40
Finn, R. A., Zaritsky, D., McCarthy, Donald W., J., et al. 2005, ApJ, 630, 206
Havlen, R. J. & Quintana, H. 1978, ApJ, 220, 14
Hudson, D. S., Mittal, R., Reiprich, T. H., et al. 2010, A&A, 513, A37
Irwin, J. A., Bregman, J. N., & Evrard, A. E. 1999, ApJ, 519, 518
Katgert, P., Mazure, A., den Hartog, R., et al. 1998, A&AS, 129, 399
Kravtsov, A. V., Vikhlinin, A., & Nagai, D. 2006, ApJ, 650, 128
Liu, A., Tozzi, P., Ettori, S., et al. 2020, A&A, 637, A58
Lodders, K. 2003, The Astrophysical Journal, 591, 1220
Łokas, E. L., Wojtak, R., Gottlöber, S., Mamon, G. A., & Prada, F. 2006, MNRAS, 367, 1463
Lovisari, L., Reiprich, T. H., & Schellenberger, G. 2015, A&A, 573, A118
McCammon, D., Almy, R., Apodaca, E., et al. 2002, ApJ, 576, 188
Merloni, A., Predehl, P., Becker, W., et al. 2012, eROSITA Science Book: Mapping the Structure of the Energetic Universe
Migkas, K., Schellenberger, G., Reiprich, T. H., et al. 2020, A&A, 636, A15
Moretti, A., Gullieuszik, M., Poggianti, B., et al. 2017, A&A, 599, A81
Navarro, J. F., Frenk, C. S., & White, S. D. M. 1997, ApJ, 490, 493
Piffaretti, R., Arnaud, M., Pratt, G. W., Pointecouteau, E., & Melin, J. B. 2011, A&A, 534, A109
Predehl, P., Andritschke, R., Arefiev, V., et al. 2021, Astronomy & Astrophysics, 647, A1
Quintana, H. & Ramirez, A. 1995, ApJS, 96, 343
Ramos-Ceja, M. E., Pacaud, F., Reiprich, T. H., et al. 2019, A&A, 626, A48
Reiprich, T. H., Basu, K., Ettori, S., et al. 2013, Space Science Reviews, 177, 195–245
Reiprich, T. H., Veronica, A., Pacaud, F., et al. 2021, A&A, 647, A2
Sanders, J. S. 2006, MNRAS, 371, 829
Schellenberger, G., Reiprich, T. H., Lovisari, L., Nevalainen, J., & David, L. 2015, A&A, 575, A30
Smith, R. J., Hudson, M. J., Nelan, J. E., et al. 2004, AJ, 128, 1558
Smith, R. K., Brickhouse, N. S., Liedahl, D. A., & Raymond, J. C. 2001, ApJ, 556, L91
Struble, M. F. & Rood, H. J. 1999, ApJS, 125, 35
Wang, Y., Xu, H., Gu, L., et al. 2010, MNRAS, 403, 1909
Willingale, R., Starling, R. L. C., Beardmore, A. P., Tanvir, N. R., & O'Brien, P. T. 2013, MNRAS, 431, 394
Wilms, J., Allen, A., & McCray, R. 2000, ApJ, 542, 914

Appendix A: Lightcurves

Fig. A.1 and A.2 show the light curves of the remaining six telescopes with a binning of 100 s in the 6 − 9 keV energy range. The presence of a flare between 37 − 43 is visible in most of the light curves as well as the excluded time periods during which the FWC data was observed for each telescope.

Appendix B: Ratio Plot

Fig. B.1 shows the ratio plot of the profiles comparing eROSITA and *Chandra* results.

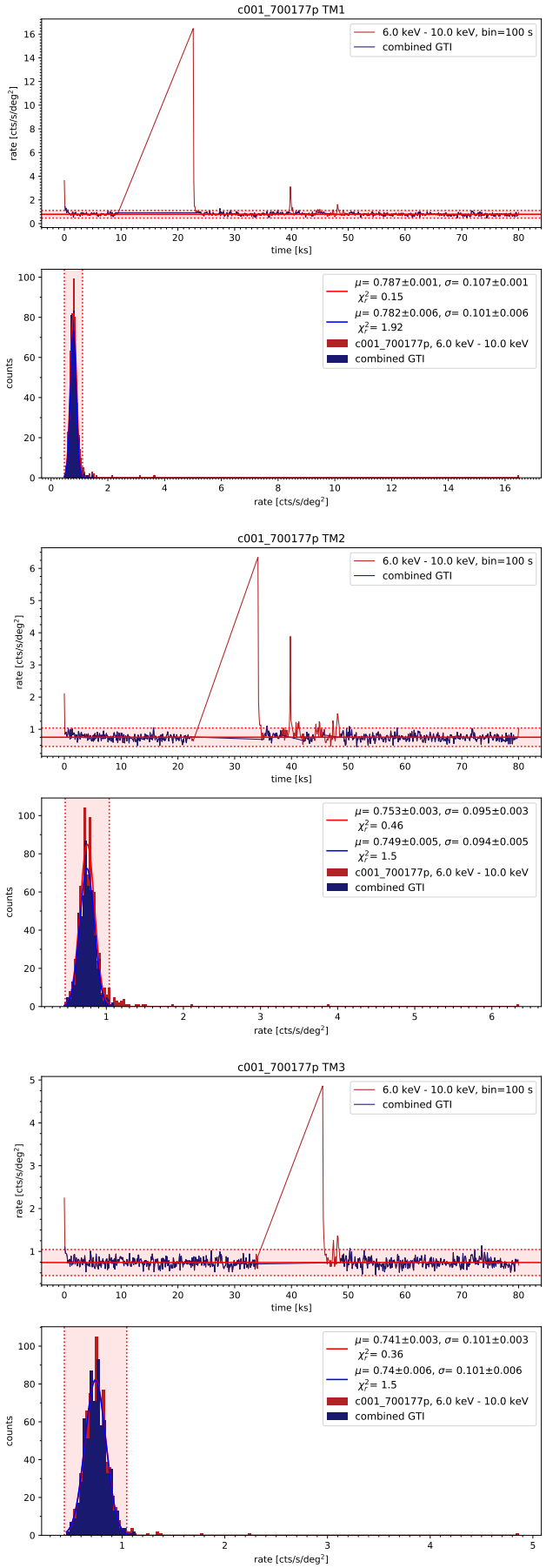

Fig. A.1. Lightcurves of TMs 1, 2, and 3.

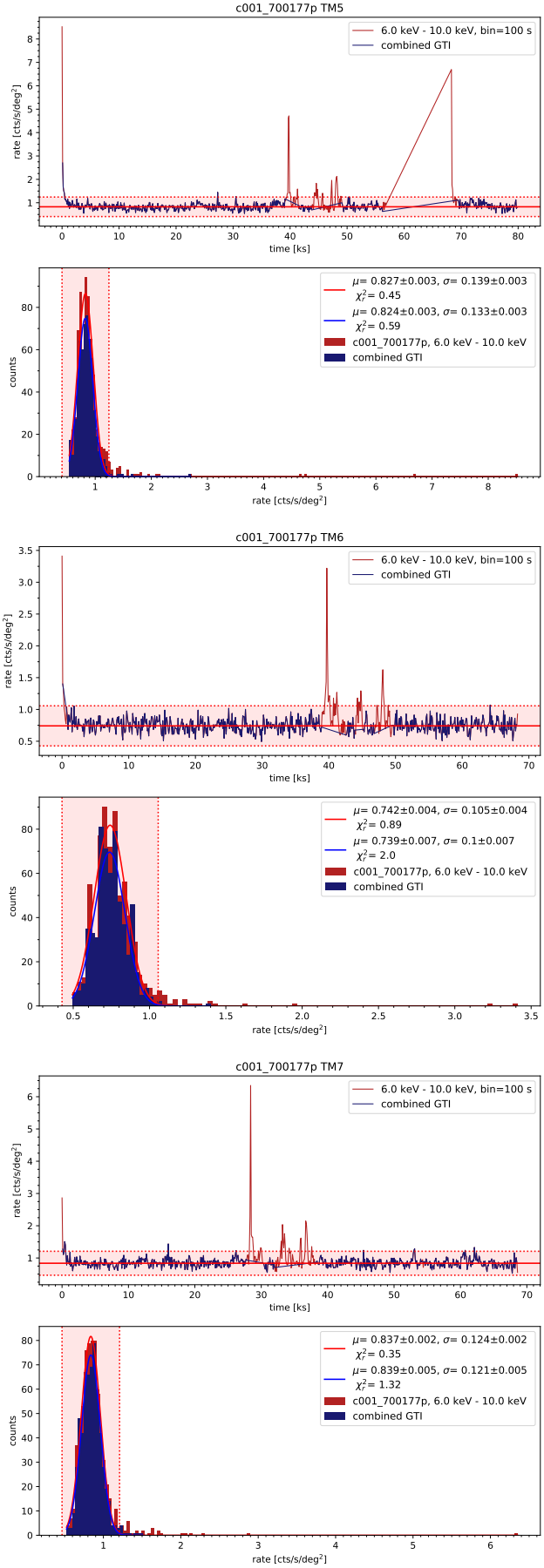

Fig. A.2. Lightcurves of TMs 5, 6, and 7

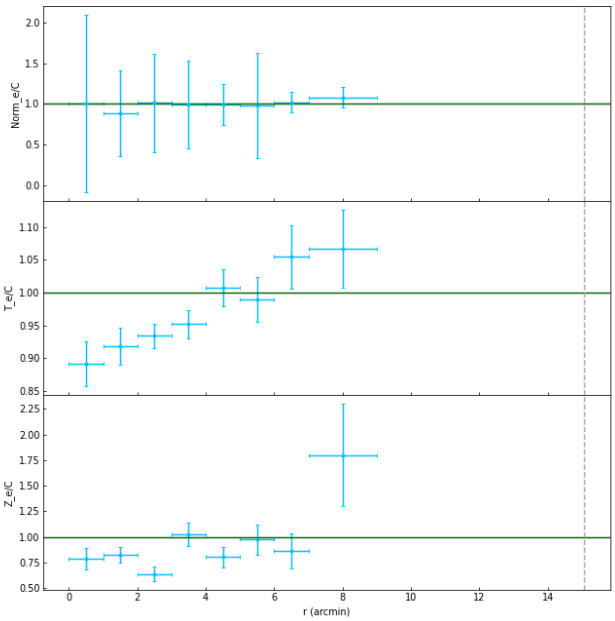

Fig. B.1. Plot of the normalisation, temperature and abundance ratios of eROSITA/*Chandra*. The grey dashed vertical line is the r_{500} of the cluster.